

Electrical Detection of Acoustic Antiferromagnetic Resonance in Compensated Synthetic Antiferromagnets

Chong Chen, Peisen Liu[✉], Shixuan Liang, Yichi Zhang, Wenxuan Zhu, Lei Han, Qian Wang, Sulei Fu, Feng Pan[✉], and Cheng Song^{✉*}

Key Laboratory of Advanced Materials, School of Materials Science and Engineering, Tsinghua University, Beijing 100084, China

 (Received 15 January 2024; revised 6 April 2024; accepted 26 June 2024; published 30 July 2024)

Compensated synthetic antiferromagnets (SAFs) stand out as promising candidates to explore various spintronic applications, benefitting from high precession frequency and negligible stray field. High-frequency antiferromagnetic resonance in SAFs, especially the optic mode (OM), is highly desired to attain fast operation speed in antiferromagnetic spintronic devices. SAFs exhibit ferromagnetic configurations above saturation field; however in that case, the intensity of OM is theoretically zero and hard to be detected in well-established microwave resonance experiments. To expose the hidden OM, the exchange symmetry between magnetic layers must be broken, inevitably introducing remanent magnetization. Here, we experimentally demonstrate a feasible method to break the symmetry via surface acoustic waves with the maintenance of compensated SAF structure. By introducing an out-of-plane strain gradient inside the Ir-mediated SAFs, we successfully reveal the hidden OM. Remarkably, the OM intensity can be effectively modulated by controlling strain gradients in SAFs with different thicknesses, confirmed by finite-element simulations. Our findings provide a feasible scheme for detecting the concealed OM, which would trigger future discoveries in magnon-phonon coupling and hybrid quasiparticle systems.

DOI: [10.1103/PhysRevLett.133.056702](https://doi.org/10.1103/PhysRevLett.133.056702)

In synthetic antiferromagnet (SAF), the antiferromagnetic coupling between ferromagnetic layers is mediated by a nonmagnetic spacer through the Ruderman-Kittel-Kasuya-Yosida interaction [1,2]. SAF inherits the strengths of both antiferromagnets and ferromagnets including high precession frequency, small stray field, convenient manipulation, and detection, which ensure SAF a promising candidate in spintronic applications such as magnetic random-access memories [3]. Owing to the antiferromagnetic interlayer coupling, there are two magnetization precession modes in SAFs: in-phase acoustic mode (AM) and out-of-phase optical mode (OM) [4,5]. In fact, the impact of driving fields on the magnetization precession is cancelled for OM excitation in the ferromagnetic configuration of SAF above saturation field due to the exchange symmetry, making it hard to detect such OM via microwave resonance experiments [6,7]. This obstacle hinders the exploration of intrinsic antiferromagnetic resonance (AFMR) in compensated SAFs, limiting its practical application in high-frequency devices. To overcome this shortcoming, asymmetric structures including different thicknesses or materials, are exploited to break the symmetry [8]. Unfortunately, the asymmetric structure will introduce remanent magnetization, which is undesired in highly integrated memory devices.

Owing to the advantages of energy-efficient excitation and detection, inherently low propagation attenuation, and suitability for miniaturization and integration, surface acoustic wave (SAW) technology has achieved great success in the industrial field, most notably for radio frequency (rf) bandpass filters in mobile communications [9]. From the perspective of fundamental research, SAW carries long-range propagating coherent phonons and constructs a versatile platform for advancing the forefront of fundamental physics [10,11]. Although noticed by the magnetism community relatively late, SAW has rapidly proven its power in the investigations of magnetism [12–14] via well-established magneto-acoustic coupling mechanisms [15,16] rather than direct magnetic sensing or mapping, for example in SAW-driven magnetization dynamics [17,18] and switching [19], as well as in nonreciprocal propagation of SAW for magneto-acoustic isolators [20–22].

Here, we exploit SAWs to observe OM precession in ferromagnetic configurations in compensated SAFs, which benefits from the out-of-plane attenuation of SAWs to break the symmetry. The strain gradients along the thickness direction have been demonstrated to generate pure spin currents via spin-rotation coupling in Cu films [23]. By anisotropic magnetoresistance (AMR) rectification, we succeeded in observing the electrical signal of OM contributed by the precession of uncancelled dynamic magnetization, also accompanied by the signal of AM. Such an insight into

*Contact author: songcheng@mail.tsinghua.edu.cn

acoustic AFMR is not only useful to monitor and modulate magnon-phonon coupling in compensated SAFs, but also provides enlightenment for novel hybrid quasiparticle systems to advance quantum information technologies.

We start by discussing our design to realize the electrical detection of acoustic AFMR in the magneto-acoustic hybrid device, as schematically shown in Fig. 1(a). As SAW passes through the SAF stripe, a microscopic earthquake occurs in it and causes its deformation. By magneto-elastic coupling, these dynamic strains can be converted into effective driving fields, asymmetrically acting on the magnetic moments of the top (FMa) and bottom (FMb) ferromagnetic layers, leading to different precession amplitudes among them. We show two AFMR modes arising from in-phase (AM) or out-of-phase (OM) precession of the two macrospins (M_a and M_b) in FMa and FMb at the ferromagnetic configuration above the saturation field. Then we move on to the electrical detection of AFMR modes. The resistance of the stripe fluctuates as magnetizations oscillate due to the presence of AMR. An rf current j_{RF} induced by the leaky electromagnetic wave whose electric field component is transversely

polarized [24,25] flowing through the stripe along the y axis is coupled to the time-dependent resistance to generate a rectified voltage across the stripe [26–28]. Details about detection principles and the origin of the rf current are presented in Supplemental Material, Sec. 1 and Sec. 2 [29]. This rectified voltage is recorded by a nanovoltmeter while an external magnetic field H is swept along the direction with an in-plane azimuthal angle φ_H relative to the x axis, to obtain acoustic AFMR spectra.

According to the well-established AFMR model in SAF [5], we calculated the resonance frequencies of the two modes in Fig. 1(b) with typical parameters in experimental samples. The magnetizations show two configurations—the canted and ferromagnetic configuration. Generally, in compensated SAF the intensity of OM in the ferromagnetic configuration is theoretically zero, as indicated by the blue dashed line. Here, we employ SAW with a matching center frequency f (horizontal gray line) to excite the hidden OM at their intersection by introducing strain gradients to break the symmetry. Finite-element method (FEM) simulations were conducted to quantitatively demonstrate the inhomogeneous strain distribution within SAFs. Figure 1(c) shows a typical plot of the shear strain ϵ_{xz} within FMa and FMb, oscillating periodically along the x axis. Since the energy of SAW is confined to the surface and it decays exponentially as the depth of penetration increases, strains within SAF are inhomogeneous across its thickness. This is the reason why there is a difference in ϵ_{xz} between FMa and FMb. All the strain components within FMa and FMb and their differences can be found in the Supplemental Material, Sec. 3 [29]. Considering that SAF thickness is much smaller than the penetration depth of SAW (order of magnitude of wavelength $\sim 1 \mu\text{m}$), ϵ_{xz} decreases approximately linearly while moving away from the substrate surface in Fig. 1(d). ϵ_{xz} is close to zero at the surface of SAF, but its value will not be equal to zero. This result is also applicable in thicker samples. The other two nonvanishing strain components (ϵ_{xx} and ϵ_{zz}) in Rayleigh SAW are also included in Fig. 1(d), exhibiting a tendency opposite to that of ϵ_{xz} . Although the thickness of SAF film is much smaller than the attenuation depth of SAW with the order of wavelength, our simulations indicate a considerable strain change in the thickness direction of SAF (see the Supplemental Material, Sec. 3) [29], which is also evidenced by the previous work [20]. Resultantly, strain gradients form along the out-of-plane direction, leading to the broken symmetry in SAF and the subsequent detection of hidden OM.

Stack structures of $\text{Ni}(t_{\text{Ni}})/\text{Ir}(0.4)/\text{Ni}(t_{\text{Ni}})$ (units in nanometer) with different Ni thickness t_{Ni} were deposited on the LiNbO_3 substrate (see the Supplemental Material, Sec. 3) [29]. The hysteresis loop of the prepared $\text{Ni}(14)/\text{Ir}(0.4)/\text{Ni}(14)$ SAF sample is depicted in Fig. 2(a) with the magnetic field H applied along $\varphi_H = 0^\circ$. When H decreases from the saturated state, the magnetization is

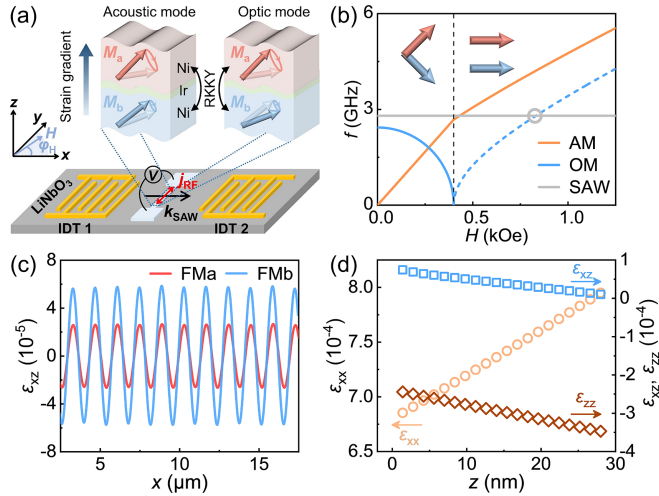


FIG. 1. (a) Schematic of the investigated magneto-acoustic hybrid device and coordinate system used. IDT represents interdigital transducer to excite SAW through the inverse piezoelectric effect. The enlarged view shows the strain within SAF induced by SAW and two AFMR modes at the ferromagnetic configuration, including the acoustic and optic mode. (b) Calculated resonance frequency of AM and OM as a function of the external magnetic field H at two magnetization states including the canted and ferromagnetic configuration, which are schematically depicted by the red (M_a) and blue (M_b) arrows. (c) Spatial distributions of shear strain ϵ_{xz} along the x axis in FMa and FMb, calculated at $z = 23.4 \text{ nm}$ (FMa) and $z = 9 \text{ nm}$ (FMb). The surface of LiNbO_3 substrate is at $z = 0$. The simulated structure is $\text{Ir}(2)/\text{Ni}(14)/\text{Ir}(0.4)/\text{Ni}(14)/\text{Ir}(2)$ (units in nanometer). (d) Spatial distributions of the amplitude of ϵ_{xx} (orange circle), ϵ_{xz} (blue square), and ϵ_{zz} (brown diamond) along the z axis within the SAF.

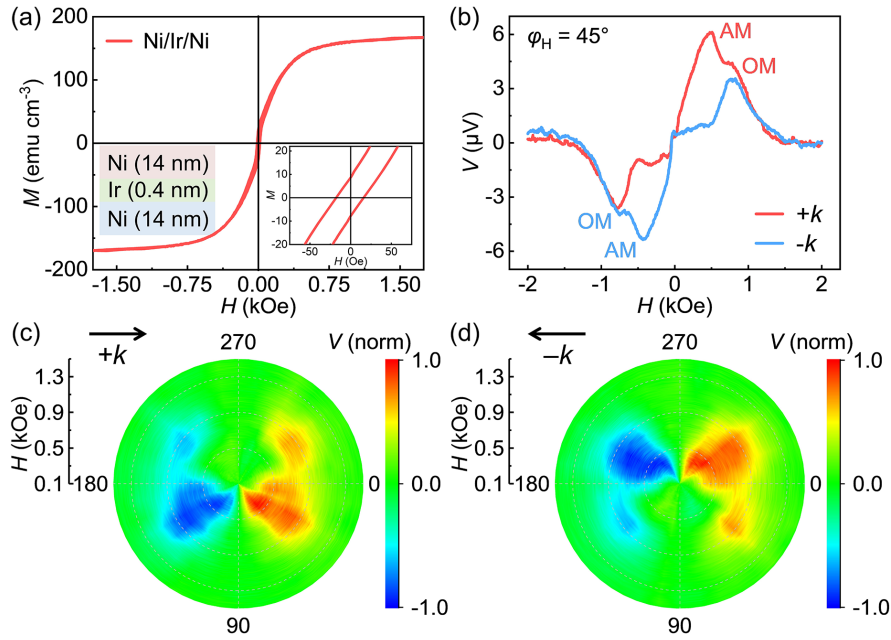


FIG. 2. (a) Hysteresis loop of Ni(14)/Ir(0.4)/Ni(14) sample with the inset showing the magnified loop near zero magnetic field, exhibiting a negligible net magnetic moment at zero field (7.9 emu cm^{-3}). (b) Magnetic field dependences of rectified voltage V at $\varphi_H = 45^\circ$ for $+k$ (red line) and $-k$ (blue line). (c)–(d) Polar plots of rectified voltage V as a function of the orientation and magnitude of the external magnetic field H for $+k$ (c) and $-k$ (d). The excitation rf frequency and power are 2.796 GHz and 19 dBm respectively.

reduced to near zero with a remanent magnetization of 7.9 emu cm^{-3} , exhibiting a negligible net moment at zero field in this compensated SAF. Figure 2(b) shows a typical acoustic AFMR spectrum in this sample measured at $\varphi_H = 45^\circ$ under the excitation of SAWs, propagating along the $+x$ direction ($+k$) and $-x$ direction ($-k$). Resonance peaks appear at specific magnetic fields where the frequencies of magnetization precession modes match that of SAW. Note that two well-resolved resonance peaks are clearly distinguishable under positive H for $+k$, corresponding to AM and OM, respectively. But there is only one resonance peak of OM under negative H without the appearance of AM. When SAW travels with $-k$, the two resonance peaks appear at negative H . As a control experiment, we performed the same measurements on samples without antiferromagnetic coupling, including a ferromagnetic coupled multilayer and single ferromagnetic layer. We can see only one AM resonance peak (see the Supplemental Material, Sec. 4) [29], suggesting that the OM in Fig. 2(b) arises from antiferromagnetic coupling.

Figure 2(c) summarizes the field-dependent voltages at different angles φ_H for $+k$. Resonances occur in all four quadrants (four voltage maxima/minima in the circle), which is qualitatively consistent with the prior reports of acoustic AFMR in layered crystalline antiferromagnet CrCl_3 [40]. However, the coexistence of two resonance peaks only occurs with H at $0^\circ < \varphi_H < 180^\circ$, namely, the broader resonance field ranges in the first and second quadrants. In comparison, for SAW traveling with $-k$ in Fig. 2(d), the tendency of the angle-dependent voltage is

just the opposite. These data demonstrate the nonreciprocal voltage in acoustic AFMR spectra.

We now proceed to the quantitative characterization of the resonance modes from acoustic AFMR spectra in the sample above. Figure 3(a) shows a typical acoustic AFMR spectrum measured at $\varphi_H = 45^\circ$ with $+k$ SAW excitation. To extract the intensity of AM and OM, the resonance curve is decomposed into AM and OM components with the following Lorentz fitting:

$$V(H) = V_{\text{AM}} \frac{(\Delta H_A)^2}{(\Delta H_A)^2 + (H - H_A)^2} + V_{\text{OM}} \frac{(\Delta H_O)^2}{(\Delta H_O)^2 + (H - H_O)^2}, \quad (1)$$

where $V_{\text{AM(OM)}}$, $\Delta H_{\text{A(O)}}$ and $H_{\text{A(O)}}$ represent intensity, linewidth, and resonance field of the resonance peak of AM(OM), respectively.

To demonstrate that the resonance peaks in Fig. 3(a) are definitely derived from AFMR, we fabricated SAW devices with different center frequencies f to study the frequency dependence of resonance. The acoustic AFMR spectra obtained at different SAW frequencies are presented in Fig. 3(b). As the frequency decreases, peak positions of the two resonance peaks gradually shift toward the zero-field direction. The resonance fields can be extracted at each frequency according to Eq. (1), and their dependences on frequency are plotted in Fig. 3(c). Considering negligible anisotropy in this sample (see the Supplemental Material, Sec. 3) [29], the dispersion

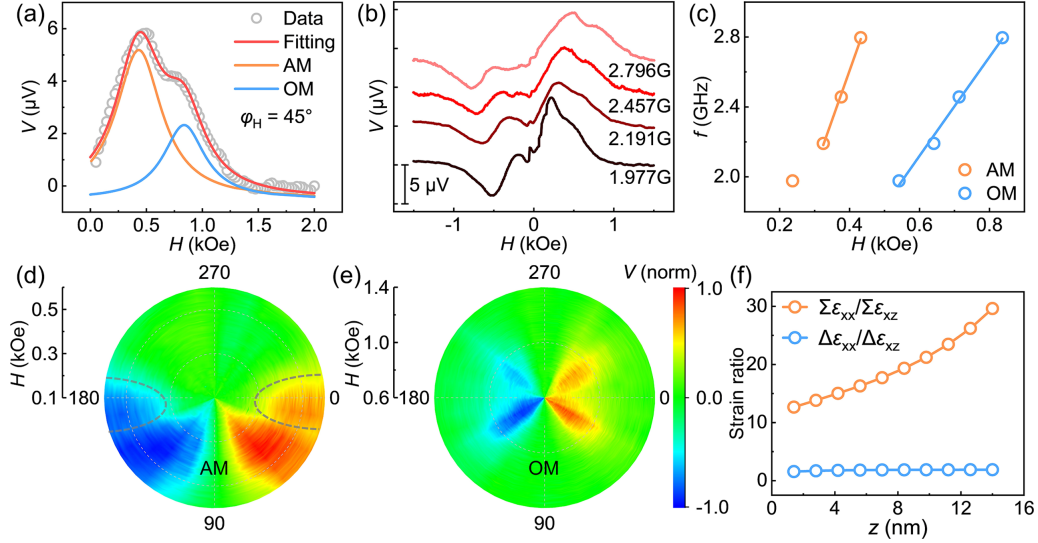


FIG. 3. (a) Acoustic AFMR spectrum consisting of AM and OM signals measured at $\varphi_H = 45^\circ$ for $+k$. (b) Frequency dependence of acoustic AFMR spectrum at $\varphi_H = 45^\circ$ for $+k$. The rf power is fixed to be 19 dBm for all the frequencies. (c) SAW frequency f as a function of resonance fields. (d)–(e) Polar plots of voltage V as a function of the orientation and magnitude of H for separate AM (d) and OM (e). (f) Spatial distributions of strain ratios, including $\Sigma\epsilon_{xx}/\Sigma\epsilon_{xz}$ and $\Delta\epsilon_{xx}/\Delta\epsilon_{xz}$, along the z axis, where Σ and Δ represent the sum and difference of corresponding strains in FMA and FMB respectively.

relationship between f and $H_{A(O)}$ can be fitted by the well-known formulas for AFMR in the easy-plane SAF of ferromagnetic configuration [5]:

$$\text{AM: } f = \frac{\gamma}{2\pi} \sqrt{H_A(H_A + 4\pi M_{\text{eff}})} \quad (2)$$

$$\text{OM: } f = \frac{\gamma}{2\pi} \sqrt{(H_O - 2H_{\text{AF}})(H_O + 4\pi M_{\text{eff}} - 2H_{\text{AF}})}, \quad (3)$$

where γ , M_{eff} , and H_{AF} indicate gyromagnetic ratio, effective magnetization, and antiferromagnetic coupling field, respectively. The fitted $\gamma/2\pi$, $4\pi M_{\text{eff}}$, and $2H_{\text{AF}}$ are determined to be 2.76 GHz kOe $^{-1}$, 0.79 kOe, and 0.41 kOe. Notice that there is an orange circle around 2 GHz that deviates from the fitting curve. This is because as the SAW frequency decreases, the smaller resonance field puts the magnetization in the canted configuration. Such frequency just matches OM in the canted configuration and excites its resonance. Also in our samples, the dipolar field originating from acoustic spin wave resonance has little effect on the dispersion relationship and has been ignored in the equations above (see the Supplemental Material, Sec. 5) [29]. This fitting shows that the resonance peaks arise from AFMR, which is driven by SAW. Similar results are also obtained in the sample with $t_{\text{Ni}} = 10$ nm (see the Supplemental Material, Sec. 6) [29].

To understand the nonreciprocal coupling between the SAW and AFMR mode in greater detail, we need to analyze the angle-dependent acoustic AFMR spectra. AM and OM were decomposed, and their respective angle dependencies are summarized in Figs. 3(d) and 3(e) respectively. Both

AM and OM exhibit nonreciprocal characteristics, which is reflected by a larger voltage with H at $0^\circ < \varphi_H < 180^\circ$ than that with H in the opposite direction ($\varphi_H + 180^\circ$). The nonreciprocity of AM and OM only shows an asymmetry in the amplitude of the resonance peak, which is based on a helicity mismatch between the driving field and magnetization precession [41]. The most notable feature is that AM has stronger nonreciprocity than OM at their respective resonance fields. Obviously, for AM the resonant signal at $180^\circ < \varphi_H < 360^\circ$ is almost completely suppressed, leaving only the signal at $0^\circ < \varphi_H < 180^\circ$. But for OM, the nonreciprocity is not so significant. In previous work on AMR rectification detection of acoustic ferromagnetic resonance [24], the nonreciprocity in rectified voltage, originating from the helicity mismatch effect, shows a positive correlation with the ratio of the in-plane and out-of-plane driving field, i. e., the ratio of longitudinal and shear strain. Via FEM simulations in Fig. 3(f), we find that the strain ratio $\Sigma\epsilon_{xx}/\Sigma\epsilon_{xz}$ which determines the strength of nonreciprocity in AM is much larger than $\Delta\epsilon_{xx}/\Delta\epsilon_{xz}$ which determines that in OM, generating a more significant nonreciprocity in AM. In addition, it is worth mentioning that there are resonant signals near 0° and 180° in Fig. 3(d) (enclosed by the dashed lines), most likely contributed by the gyromagnetic effect [18]. The angle dependence of the intensity of the ferromagnetic resonance driven by the gyromagnetic field shows twofold symmetry and reaches its extreme values at $\varphi_H = n\pi$, namely, the resonant signals near 0° and 180° in our configuration (see the Supplemental Material, Sec. 7) [29].

Finally, we show that the intensity of OM can be modulated by changing the thickness of the Ni layer.

Figure 4(a) displays typical acoustic AFMR spectra in samples with different Ni thicknesses, and the thickness t_{Ni} is labeled near the corresponding curve. Two well-resolved resonance peaks can be clearly distinguished from $t_{\text{Ni}} = 8$ nm to 18 nm. The blue vertical dashed line marks the resonance peaks of OM. When reaching 20 nm, the OM can no longer be resolved. The antiferromagnetic coupling field becomes weaker with increasing t_{Ni} . Also, the larger linewidth at $t_{\text{Ni}} = 20$ nm hinders our extraction of OM. Additionally, note that there is no resonance signal in the sample with $t_{\text{Ni}} = 5$ nm, probably due to the low crystallinity and weak magnetization of the ultrathin Ni film (see the Supplemental Material, Sec. 3) [29]. For the sample with $t_{\text{Ni}} = 12$ nm, we present its resonance curve measured at $\varphi_{\text{H}} = 45^\circ$ in Fig. 4(b), which is decomposed into AM and OM components according to Eq. (1). We can find that the intensity of OM is significantly suppressed compared with the $t_{\text{Ni}} = 14$ nm counterpart in Fig. 3(a). Then all the AM and OM components in each SAF sample ($8 \text{ nm} \leq t_{\text{Ni}} \leq 18 \text{ nm}$) can be extracted, and their ratios $V_{\text{OM}}/V_{\text{AM}}$ are summarized in Fig. 4(c). Note that $V_{\text{OM}}/V_{\text{AM}}$, reflecting the relative intensity of OM, shows a strong dependence on t_{Ni} . As t_{Ni} increases, the value of $V_{\text{OM}}/V_{\text{AM}}$ enhances monotonously and approaches saturation at $t_{\text{Ni}} = 14$ nm, which is ascertained to be 0.5. This thickness dependence of the OM strength can be well explained by establishing a link with the strain inside the SAF. $V_{\text{OM}}/V_{\text{AM}}$ can be modeled and derived by the following equation (see the Supplemental Material, Sec. 1) [29]:

$$\frac{V_{\text{OM}}}{V_{\text{AM}}} \propto \frac{(\varepsilon_{\text{xx}}^{\text{a}} - \varepsilon_{\text{xx}}^{\text{b}}) - (\varepsilon_{\text{xz}}^{\text{a}} - \varepsilon_{\text{xz}}^{\text{b}})}{(\varepsilon_{\text{xx}}^{\text{a}} + \varepsilon_{\text{xx}}^{\text{b}}) - (\varepsilon_{\text{xz}}^{\text{a}} + \varepsilon_{\text{xz}}^{\text{b}})}, \quad (4)$$

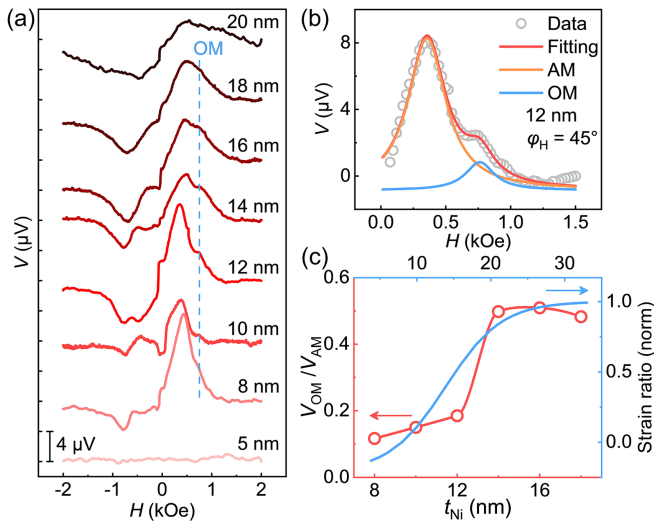


FIG. 4. (a) Magnetic field dependences of voltage V at $\varphi_{\text{H}} = 45^\circ$ in $\text{Ni}(t_{\text{Ni}})/\text{Ir}(0.4)/\text{Ni}(t_{\text{Ni}})$ SAF with different t_{Ni} (5 ~ 20 nm) for $+k$. (b) Acoustic AFMR spectrum measured at $\varphi_{\text{H}} = 45^\circ$ in the sample with $t_{\text{Ni}} = 12$ nm under $+k$ SAW excitation, decomposing into AM and OM components. (c) Ratios of fitting coefficients $V_{\text{OM}}/V_{\text{AM}}$ and normalized strain in SAFs with different t_{Ni} .

where $\varepsilon_{\text{xx}}^{\text{a(b)}}$ and $\varepsilon_{\text{xz}}^{\text{a(b)}}$ represent the longitudinal and shear strain in FMa (FMb). FEM simulations can give the strain ratio on the right-hand side of Eq. (4). The results of normalized strain ratio are also included in Fig. 4(c). The value in the sample with $t_{\text{Ni}} = 12$ nm is less than that in the sample with $t_{\text{Ni}} = 14$ nm, which accounts for the suppression of OM in Fig. 4(b). The simulated strain ratio and experimental OM relative intensity follow the same trend with t_{Ni} , namely they both rise monotonically and then converge to a saturation value, which proves the validity of our theoretical model. It is worth mentioning that they reach saturation at different t_{Ni} values. The reason may come from strain relaxation in the prepared film, which is difficult to be taken into account in the FEM simulations.

In conclusion, we have experimentally demonstrated that acoustic AFMR, especially the OM in ferromagnetic configuration, can be electrically detected via an out-of-plane strain gradient in compensated SAF, which provides an alternative approach to break the symmetry in it. By simple line shape analysis of acoustic AFMR spectra, we have distinctly extracted the voltage signals contributed by AM and OM respectively. The uncompensated magnetization precessions in the top and bottom ferromagnetic layers result in a distinguishable OM signal. Angle-dependent experiments show that AM has a greater non-reciprocity than OM, which is attributed to the greater strain ratio contributing to AM. The relative intensity of OM can be further modulated by changing the thickness of the ferromagnetic layer. By FEM simulations, we find that the modulation of OM intensity derives from different normalized strain ratios at different thicknesses. The normalized strain ratio shows a positive correlation with the OM intensity, and they both converge to a saturation value. Our findings demonstrate a completely new way to introduce broken symmetry and unravel the concealed OM in compensated SAFs, which helps to advance the burgeoning field of magneto-acoustic coupling devices.

Acknowledgments—This work is supported by the National Natural Science Foundation of China (Grants No. 52225106, No. 12241404, and No. T2394470), the National Key Research and Development Program of China (Grant No. 2022YFA1402603), and the Natural Science Foundation of Beijing (Grant No. JQ20010). Some devices were fabricated via an Ultraviolet Maskless Lithography machine (model: UV Litho-ACA, TuoTuo Technology).

- [1] S. S. P. Parkin, Systematic variation of the strength and oscillation period of indirect magnetic exchange coupling through the 3d, 4d, and 5d transition metals, *Phys. Rev. Lett.* **67**, 3598 (1991).

- [2] R. Chen *et al.*, Reducing Dzyaloshinskii-Moriya interaction and field-free spin-orbit torque switching in synthetic antiferromagnets, *Nat. Commun.* **12**, 3113 (2021).
- [3] D. Apalkov, B. Dieny, and J. M. Slaughter, Magnetoresistive random access memory, *Proc. IEEE* **104**, 1796 (2016).
- [4] Y. Shiota, T. Taniguchi, M. Ishibashi, T. Moriyama, and T. Ono, Tunable magnon-magnon coupling mediated by dynamic dipolar interaction in synthetic antiferromagnets, *Phys. Rev. Lett.* **125**, 017203 (2020).
- [5] X. Chen, C. Zheng, S. Zhou, Y. Liu, and Z. Zhang, Ferromagnetic resonance modes of a synthetic antiferromagnet at low magnetic fields, *J. Phys. Condens. Matter* **34**, 015802 (2022).
- [6] Z. Zhang, L. Zhou, P. E. Wigen, and K. Ounadjela, Using ferromagnetic resonance as a sensitive method to study temperature dependence of interlayer exchange coupling, *Phys. Rev. Lett.* **73**, 336 (1994).
- [7] A. You, M. A. Y. Be, and I. In, Studies of coupled metallic magnetic thin-film trilayers, *J. Appl. Phys.* **84**, 958 (1998).
- [8] G. Wu, S. Chen, Y. Ren, Q. Y. Jin, and Z. Zhang, Laser-induced magnetization dynamics in interlayer-coupled $[\text{Ni}/\text{Co}]_4/\text{Ru}/[\text{Co}/\text{Ni}]_3$ perpendicular magnetic films for information storage, *ACS Appl. Nano Mater.* **2**, 5140 (2019).
- [9] R. Su *et al.*, Wideband and low-loss surface acoustic wave filter based on $15^\circ\text{YX} - \text{LiNbO}_3/\text{SiO}_2/\text{Si}$ structure, *IEEE Electron Device Lett.* **42**, 438 (2021).
- [10] M. Yokoi, S. Fujiwara, T. Kawamura, T. Arakawa, K. Aoyama, H. Fukuyama, K. Kobayashi, and Y. Niimi, Negative resistance state in superconducting NbSe_2 induced by surface acoustic waves, *Sci. Adv.* **6**, eaba1377 (2020).
- [11] J. Wang *et al.*, Generation of a single-cycle acoustic pulse: A scalable solution for transport in single-electron circuits, *Phys. Rev. X* **12**, 031035 (2022).
- [12] W. G. Yang and H. Schmidt, Acoustic control of magnetism toward energy-efficient applications, *Appl. Phys. Rev.* **8**, 021304 (2021).
- [13] J. Puebla, Y. Hwang, S. Maekawa, and Y. Otani, Perspectives on spintronics with surface acoustic waves, *Appl. Phys. Lett.* **120**, 220502 (2022).
- [14] C. Chen, M.-Y. Ma, F. Pan, and C. Song, Magneto-acoustic coupling: Physics, materials, and devices, *Acta Phys. Sin.* **73**, 058502 (2024).
- [15] L. Dreher, M. Weiler, M. Pernpeintner, H. Huebl, R. Gross, M. S. Brandt, and S. T. B. Goennenwein, Surface acoustic wave driven ferromagnetic resonance in nickel thin films: Theory and experiment, *Phys. Rev. B* **86**, 134415 (2012).
- [16] M. Matsuo, J. Ieda, K. Harii, E. Saitoh, and S. Maekawa, Mechanical generation of spin current by spin-rotation coupling, *Phys. Rev. B* **87**, 180402(R) (2013).
- [17] M. Weiler, L. Dreher, C. Heeg, H. Huebl, R. Gross, M. S. Brandt, and S. T. B. Goennenwein, Elastically driven ferromagnetic resonance in nickel thin films, *Phys. Rev. Lett.* **106**, 117601 (2011).
- [18] Y. Kurimune, M. Matsuo, and Y. Nozaki, Observation of gyromagnetic spin wave resonance in NiFe films, *Phys. Rev. Lett.* **124**, 217205 (2020).
- [19] W. Al Misba, M. M. Rajib, D. Bhattacharya, and J. Atulasimha, Acoustic-wave-induced ferromagnetic-resonance-assisted spin-torque switching of perpendicular magnetic tunnel junctions with anisotropy variation, *Phys. Rev. Appl.* **14**, 014088 (2020).
- [20] M. Kü, M. Heigl, L. Flacke, A. Hörner, M. Weiler, M. Albrecht, and A. Wixforth, Nonreciprocal Dzyaloshinskii-Moriya magnetoacoustic waves, *Phys. Rev. Lett.* **125**, 217203 (2020).
- [21] L. Liao, J. Puebla, K. Yamamoto, J. Kim, S. Maekawa, Y. Hwang, Y. Ba, and Y. Otani, Valley-selective phonon-magnon scattering in magnetoelastic superlattices, *Phys. Rev. Lett.* **131**, 176701 (2023).
- [22] M. Küß, S. Glamsch, Y. Kunz, A. Hörner, M. Weiler, and M. Albrecht, Giant surface acoustic wave nonreciprocity with low magnetoacoustic insertion loss in $\text{CoFeB}/\text{Ru}/\text{CoFeB}$ synthetic antiferromagnets, *ACS Appl. Electron. Mater.* **5**, 5103 (2023).
- [23] D. Kobayashi, T. Yoshikawa, M. Matsuo, R. Iguchi, S. Maekawa, E. Saitoh, and Y. Nozaki, Spin current generation using a surface acoustic wave generated via spin-rotation coupling, *Phys. Rev. Lett.* **119**, 077202 (2017).
- [24] C. Chen, L. Han, P. Liu, Y. Zhang, S. Liang, Y. Zhou, W. Zhu, S. Fu, F. Pan, and C. Song, Direct-current electrical detection of surface-acoustic-wave-driven ferromagnetic resonance, *Adv. Mater.* **35**, 2302454 (2023).
- [25] R. Iguchi and E. Saitoh, Measurement of spin pumping voltage separated from extrinsic microwave effects, *J. Phys. Soc. Jpn.* **86**, 011003 (2017).
- [26] D. Castilla, M. Muñoz, M. Sinusía, R. Yanes, and J. L. Prieto, Large asymmetry in the magnetoresistance loops of ferromagnetic nanostrips induced by surface acoustic waves, *Sci. Rep.* **11**, 8586 (2021).
- [27] X. Fan, W. Wang, Y. Wang, H. Zhou, J. Rao, X. Zhao, C. Gao, Y. S. Gui, C. M. Hu, and D. Xue, Rapid characterizing of ferromagnetic materials using spin rectification, *Appl. Phys. Lett.* **105**, 262404 (2014).
- [28] M. Obstbaum, M. Härtinger, H. G. Bauer, T. Meier, F. Swientek, C. H. Back, and G. Woltersdorf, Inverse spin Hall effect in $\text{Ni}_{81}\text{Fe}_{19}$ /Normal-Metal-Bilayers, *Phys. Rev. B* **89**, 060407(R) (2014).
- [29] See Supplemental Material at <http://link.aps.org/supplemental/10.1103/PhysRevLett.133.056702> for electrical detection principle and model description, origin of rf current j_{RF} , experimental and simulation section, control experiments in ferromagnetic coupled multilayer and single ferromagnetic layer, dispersion relationship in easy-plane SAF, acoustic AFMR spectra in the SAF with 10 nm Ni, and resonant signals near 0° and 180° , which include Refs. [1,5,7,17,19,24–26,29–38].
- [30] A. Wirthmann, X. Fan, Y. S. Gui, K. Martens, G. Williams, J. Dietrich, G. E. Bridges, and C. M. Hu, Direct phase probing and mapping via spintronic michelson interferometry, *Phys. Rev. Lett.* **105**, 017202 (2010).
- [31] M. Harder, Z. X. Cao, Y. S. Gui, X. L. Fan, and C. M. Hu, Analysis of the line shape of electrically detected ferromagnetic resonance, *Phys. Rev. B* **84**, 054423 (2011).
- [32] L. H. Bai, Y. S. Gui, A. Wirthmann, E. Recksiedler, N. Mecking, C. M. Hu, Z. H. Chen, and S. C. Shen, The rf magnetic-field vector detector based on the spin rectification effect, *Appl. Phys. Lett.* **92**, 032504 (2008).

- [33] R. Sasaki, Y. Nii, Y. Iguchi, and Y. Onose, Nonreciprocal propagation of surface acoustic wave in Ni/LiNbO₃, *Phys. Rev. B* **95**, 020407(R) (2017).
- [34] C. Chen, S. Fu, L. Han, R. Su, P. Liu, R. Chen, W. Zhu, L. Liao, F. Pan, and C. Song, Energy harvest in ferromagnet-embedded surface acoustic wave devices, *Adv. Electron. Mater.* **8**, 2200593 (2022).
- [35] X. Li, D. Labanowski, S. Salahuddin, and C. S. Lynch, Spin wave generation by surface acoustic waves, *J. Appl. Phys.* **122**, 043904 (2017).
- [36] Y. Luo, M. Moske, and K. Samwer, Interlayer coupling and magnetoresistance in Ir/Co multilayers, *Europhys. Lett.* **42**, 565 (1998).
- [37] W. He *et al.*, Anisotropic magnon-magnon coupling in synthetic antiferromagnets, *Chin. Phys. Lett.* **38**, 057502 (2021).
- [38] W. Hu, M. Huang, H. Xie, H. Zhang, and F. Bai, Self-biased magnetic field sensors based on surface acoustic waves through angle-dependent magnetoacoustic coupling, *Phys. Rev. Appl.* **19**, 014010 (2023).
- [39] S. Tateno, G. Okano, M. Matsuo, and Y. Nozaki, Electrical evaluation of the alternating spin current generated via spin-vorticity coupling, *Phys. Rev. B* **102**, 104406 (2020).
- [40] T. P. Lyons, J. Puebla, K. Yamamoto, R. S. Deacon, Y. Hwang, K. Ishibashi, S. Maekawa, and Y. Otani, Acoustically driven magnon-phonon coupling in a layered antiferromagnet, *Phys. Rev. Lett.* **131**, 196701 (2023).
- [41] M. Küß, M. Hassan, Y. Kunz, A. Hörner, M. Weiler, and M. Albrecht, Nonreciprocal transmission of magnetoacoustic waves in compensated synthetic antiferromagnets, *Phys. Rev. B* **107**, 214412 (2023).